REVIEW PAPER

CrossMark

Grain-scale characterization of water retention behaviour of sand using X-ray CT

Ghonwa Khaddour[1] · Ismael Riedel[1] · Edward Andò[2] · Pascal Charrier[1] · Pierre Bésuelle[2] · Jacques Desrues[2] · Gioacchino Viggiani[1] · Simon Salager[1]

Abstract

This paper introduces X-ray tomography as an experimental method that allows grain-scale measurements for both porosity and degree of saturation. A whole configuration and set-up were developed specifically for the study of unsaturated Hostun sand and its water retention behaviour, using X-ray CT. A "step-by-step" protocol to obtain reconstructed volumes of sufficient quality where the three phases of the specimen can be clearly distinguished (i.e., grain, water and air) was also presented. A post-processing of the images helped the visualization and the characterization of the three phases within the specimen. A region growing separation tool was used to obtain trinarized volumes, allowing a qualitative/quantitative analysis to be performed. A qualitative interpretation of the resulting images has been done focusing on the water retention domains, where images of each different domain were retrieved for different suction values. Later, local measurements of relevant soil variables were conducted for a chosen subvolume of $\approx 3 \times D_{50}$. This helped to build a map of measurement that covers the entire specimen field. Finally, water retention curve of Hostun sand was plotted and compared to a reference one. An investigation about the relation between the state variables: porosity and degree of saturation, for a constant suction, was performed. A noteworthy trend between porosity and degree of saturation was identified and discussed. The analysis presented in this study could be adapted for other granular materials, combined with pore size distribution and pore shape description, in order to understand the local relation between water retention behaviour characteristics and build a model that covers the whole retention behaviour of unsaturated granular materials.

Keywords Grain-scale analysis · Unsaturated sand · Water retention behaviour · X-ray computed tomography

1 Introduction

In nature, sand above the water table is often partially saturated, i.e., with the pore space filled with both air and water. The hydraulic behaviour of partially saturated sand is typically described by the so-called water retention curve (WRC), expressing water content (w) or degree of saturation (Sr) as a function of suction (negative pore water pressure, s), see [14, 28, 45, 48]. The macroscopic water retention behaviour of sand has been investigated in a number of studies, e.g., [5, 18, 24, 31, 35, 38, 41, 43], yielding some relation between the relevant state variables: suction, degree of saturation, and—in some cases—porosity (n). However, porosity and degree of saturation are usually measured at the sample level which in traditional testing does not allow the important issue of spatial variability to be addressed.

The key point of spatial variability (of both saturation and density) in sand has been addressed in a number of experimental studies using a number of different techniques including surface photography [51] and X-ray tomography [9, 20–22, 26, 36]. An important distinction is in the spatial resolution of the studies—some studies are performed at a level where the sand is taken as a continuum, whereas higher resolution studies are able to look at the water distribution between individual grains of sand. This grain-scale study addresses this issue using in situ X-ray tomography to follow the 3D distribution of air,

✉ Simon Salager
  simon.salager@3sr-grenoble.fr

1   Univ. Grenoble Alpes, 3SR, 38000 Grenoble, France

2   CNRS, 3SR, 38000 Grenoble, France

water and grain during drying and wetting of small specimens of sand. A grain-scale study can answer questions regarding heterogeneities (of sample density or water distribution) as well the effect that pore shape and size have on water retention. Furthermore, with an appropriately defined local porosity and degree of saturation, it may be possible to verify the meaningfulness of a locally defined water retention curve.

Besides the water retention behaviour of sand itself, the variability of degree of saturation and porosity are of key interest for the mechanical behaviour of sand, with a number of important works highlighting the first-order effect that the distribution of porosity [4, 6, 7] and the distribution of water have on the emergence of strain localization [8, 40, 41].

The paper is organized as follows: first a description of the hydraulic and X-ray imaging set-up is given. Second, we describe the tools developed to process raw 3D images into quantitative maps of air, water and grain phases. Finally, the local measurements of porosity and degree of saturation are presented and their implications are discussed.

2 Experimental methods

2.1 Material

In this work, we use Hostun sand (HN31), a reference sand in geomechanics [10, 12, 15]. Its chemical composition is principally silica ($SiO_2 > 98\%$). The grain shape is angular. The particle size distribution for Hostun sand and an SEM image of a few grains are shown in Fig. 1.

HN31 has a coefficient of uniformity, C_u of 1.7 and a D_{50} of 0.338 mm making it a poorly graded medium sand, according to the USCS classification. The maximum and minimum values of void ratio are given as $e_{max} = 1.041$ ($n_{max} = 51.0\%$) and $e_{min} = 0.648$ ($n_{min} = 39.3\%$),

corresponding to a maximum and minimum of specific weight of 1.324 and 1.599 g/cm³. Grains have a density of 2.65 g/cm³.

2.2 The micro-retention cell

A micro-retention cell was specifically designed to allow X-ray scanning, using an X-ray transparent material, PMMA. The use of a laboratory X-ray source implies a trade-off between geometric resolution and field of view. The requirement of high resolution therefore imposes a small specimen: a cylinder of 1 cm diameter and 1 cm height. Figure 2 shows the cell apparatus.

The cell, as can be seen in Fig. 2, has two parts: top (2) and bottom (3–7). These parts, once screwed together, form an air- and watertight cell. The sand specimen (7) is located between two porous stones (3); the one of the bottom having an air entry value of 500 kPa and the one of the top having a high porosity, such that water continuity from the bottom and air continuity from the top are guaranteed. Although an air entry value of 500 kPa is larger than necessary for the range of suction of interest in this study, it limits flow with the objective of avoiding hydraulic perturbations, especially during rotation for X-ray scanning. The upper part (2) includes a plate that can be removed to give access to the specimen. The lower part of the bottom porous stone is in contact with a water reservoir (6) to ensure saturation at all times. Two tubes (4 and 5) are connected to this reservoir, for entry and exit of water. These tubes are used to flush the system (force the exit of any air bubbles and ensure total initial saturation) and to apply suction (tensiometry).

2.3 Specimen preparation technique

The preparation of the specimen is a key step to ensure the initial homogeneity of the sand skeleton. To ensure that the experiment starts from a completely saturated state, sand
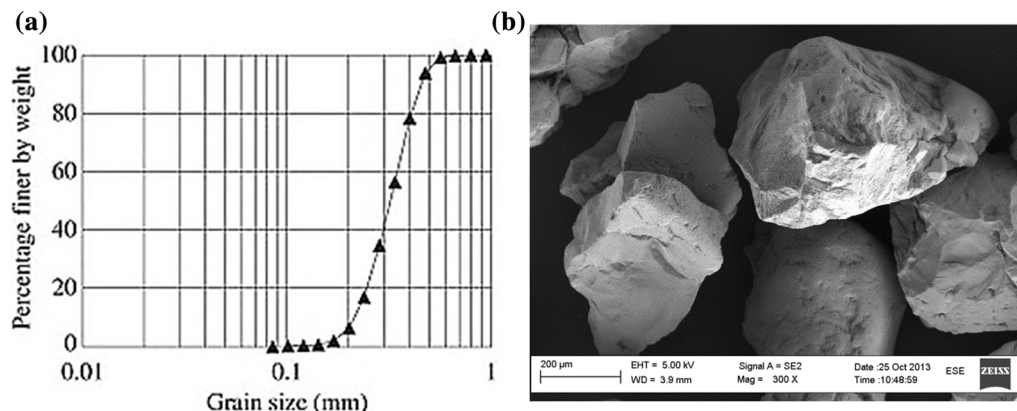

Fig. 1 **a** Grain size distribution of Hostun sand. **b** SEM image of Hostun sand courtesy of Anita Torabi

1. Air pressur access tube   3. Porous stone   6. Water reservoir
2. Removable cover   4. Water entry tube   7. Sand sample
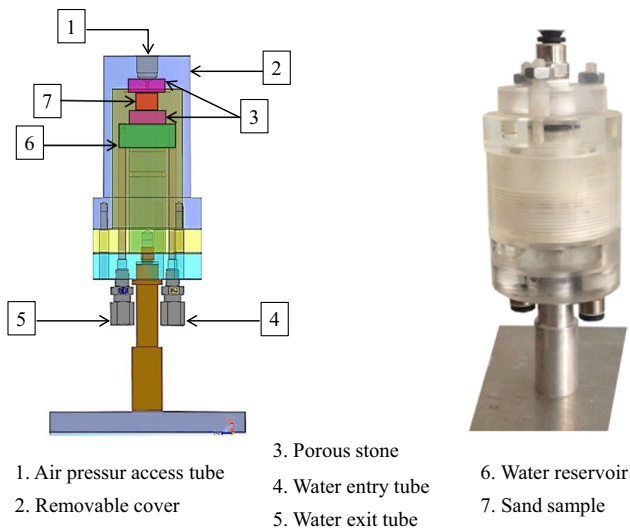   5. Water exit tube

Fig. 2 Cell and its component parts [36]

grains are pluviated (by spooning and with minimal drop height) underwater [42] with the cell completely submerged. All the (demineralized) water used in this work is de-aired for 24 h using a magnetic stirring heater and vacuum system.

2.4 Application of suction

Tensiometry is used in this work to apply suction. This method allows the application of a stable pore water pressure u_w, with an accuracy of 0.01 kPa. The largest applied suction is 7 kPa. Figure 3 shows schematically the full arrangement and illustrates how suction is applied. A water tank (3) that can move vertically over a scaled ruler is connected to the water reservoir (1) at the bottom of the cell (5). The level of top surface of the water in this tank is initially set to the zero value of the ruler at the mid-height of the sand specimen (6), $H = 0$. In this initial state, the
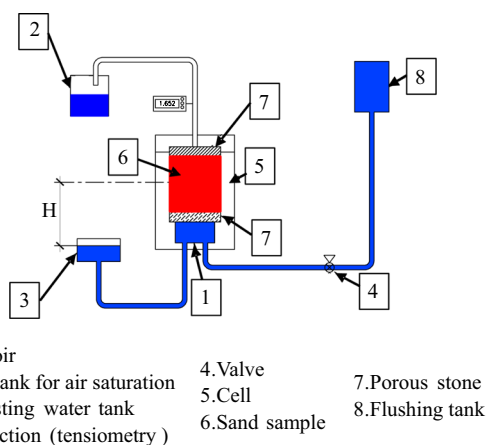
suction is equal to zero in the middle of the specimen. Moving the tank down (decreasing H) creates a water level difference and given the continuity in the liquid phase in the sand, bottom porous stone (7) and reservoir (1), suction as a negative water pressure is applied. Another porous stone (7) is placed on the top surface of the sample, with the only role of applying a small vertical stress to help prevent grains displacement at the surface.

2.5 Experimental procedure

The water retention curve of Hostun sand obtained by [32], see Fig. 4, is used as a reference. The data therein are obtained using macroscopic measurements of degree of saturation, for a drainage process, and for a void ratio equal to 0.9 ($n = 47.4\%$). An approximated air entry value (s_{air}) is given as 1.4 kPa.

After reaching the air entry value, saturation decreases rapidly with increasing suction. Different points of interest for X-ray scanning are defined (red points in Fig. 4) on this reference curve in such a way to cover all the domains (full saturation, funicular domain, pendular domain and residual saturation). The selected points are detailed in Table 1.

The protocol for this experiment is simple (but rather time consuming): first the porous stone below the specimen is saturated to ensure water continuity between the water reservoir, the porous stone and the specimen. To this end, the water reservoir in the cell is filled with water, while the bottom water exit tube is closed and a pressure of 100 kPa is imposed for 2 h (using a pressure controller) in order to force the water through the porous stone. When water drops are seen on the free side of the porous stone, it is considered to be saturated. The specimen is then deposited (as described above), and the cell installed in the X-ray scanner and connected to the suction system (described above).
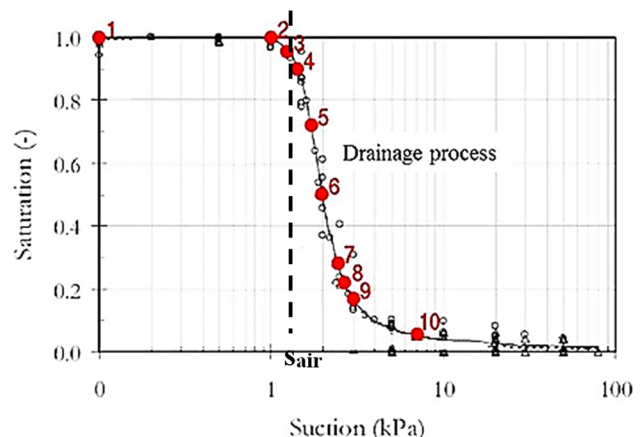

1. Water reservoir
2. Evaporation tank for air saturation
3. Vertical adjusting water tank for applying suction (tensiometry)
4. Valve
5. Cell
6. Sand sample
7. Porous stone
8. Flushing tank

Fig. 3 Sketch of the arrangement used in this work to apply suction

Fig. 4 Water retention curve for Hostun sand from [44]. The black continuous line is a fitting curve for the experimental points

Table 1 Detailed experimental programme

Scan	1	2	3	4	5	6	7	8	9	10
s (kPa)	0	1	1.2	1.4	1.8	2	2.2	2.5	3	7
Expected Sr (%) from [44]	100	99	97	94	71	50	39	28	16	5

The first X-ray scan is performed at full saturation with zero suction (red point 1 in Fig. 4). After completion of the scan, the suction corresponding to the next step is applied (as described above) waiting for three days to reach a steady state before launching the next scan (the time to reach an equilibrium state was taken from experiments by [28]). This is repeated for all steps until maximum suction. Thereafter, a last scan is performed on the specimen after drying the entire system by air convection without dismantling the cell (water weight loss was measured every 24 h until stable—10 days in this case).

After the test the cell is opened, the sand recovered, further dried in an oven for 24 h and then weighed in order to have a reference value for the solid mass.

2.6 X-ray tomography

X-ray tomography is a non-destructive, 3D imaging technique that allows the internal structure of an appropriately scanned object to be investigated [46], after acquiring radiographs from a number of different angles (in this case rotating the cell thanks to a rotation stage) and then reconstructing the field of X-ray attenuation. X-ray imaging is used herein for visualizing and quantifying water distribution in partially saturated sand specimens. The X-ray attenuation coefficient of the materials of interest (air, water and sand grains) is dependent on density, thereby giving a good contrast, especially between air and sand, see Fig. 5.
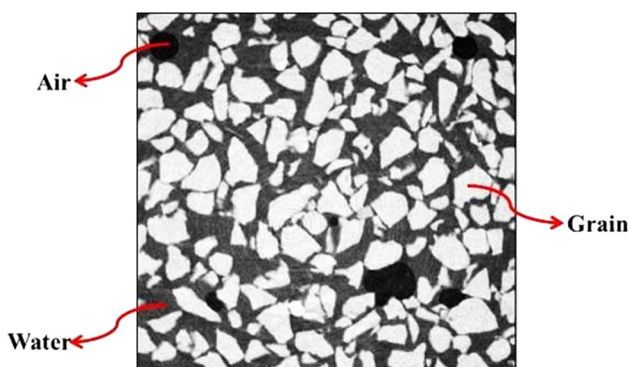

Fig. 5 Reconstructed X-ray image showing the contrast between sand grains, water and air

The experiments in this study are performed using the micro-focus X-ray tomograph in Laboratoire 3SR, Grenoble, shown in Fig. 6. See [47] for further details. The choice of a small specimen—and consequently the ability to use a small field of view—means that high geometric resolution can be obtained, in this case 7.5 μm/px, close to the maximum possible with this machine. The selection of other X-ray parameters is made to optimize image noise, scanning time and contrast. Table 2 shows the parameters used in this study.

On top of these settings, given the possibility of water rearrangement due to inertia, the system was asked to rotate the specimen as slowly as possible. At the end of a scan, lasting a little more than 2 h, the radiographs are reconstructed into a 3D volume (1500 × 1500 × 1500 voxels) using filtered back-projection [17] as implemented in Digi-CT 2.4.2 from Digisens.

3 Image processing and analysis

In order to quantify micro-water retention in 3D, the series of volumes resulting from the repeated scans at different levels of suction are trinarized into maps where each voxel is unambiguously assigned to a phase (air, water, grain, outside) using a region-growing-type segmentation (fully detailed in [19, 22] and [49] for review on segmentation methods), followed by a hole filling step in zones of intermediate Sr. The results of this treatment are first presented in detail for one 3D volume (the one selected corresponds to scan number 6, at a value of suction of 2 kPa and an expected degree of saturation of 50%).

Figure 7a shows horizontal slices taken at three different vertical positions (marked on Fig. 7c) from the greyscale-reconstructed volumes (i.e., before trinarization). There are different distributions of grain, water and air in each slice, and each slice presents a zoomed inset. These slices are to be compared with those in Fig. 7b, which presents slices in the same positions after trinarization (which allows the application of a colour map showing air in black, water in blue and grains in orange). The trinarization procedure adopted appears to correctly identify each phase (with respect to 7a) and does not appear to be very vulnerable to the artefacts due to partial volume which afflict unrefined approaches. Figure 7c presents a central vertical slice showing the inhomogeneous distribution of water within the specimen, in the form of patches and layers. On this slice, three layers can be distinguished by eye over the height of the specimen. The upper and lower layers retain a larger volume of water compared to the middle one.

Figure 8 presents horizontal and vertical slices for different values of suction ($s = 0, 1, 1.2, 1.4, 1.8, 2, 2.2, 2.5, 3$

Fig. 6 X-ray tomograph in Laboratoire 3SR: (left) a picture of the cabin, (right) the inside of the cabin with the micro-retention cell in place

Table 2 Parameters used for X-ray scanning

Parameter	Value
Source voltage	100 kV
Source current	50 μA
Number of angular positions [0°–360°]	1200
Number of images averaged at each angular position	5 or 6
Single image exposure	1

and 7 kPa), corresponding to different water retention domains.

The results show that, for the saturated case, $s = 0$ kPa, no air presence can be noticed, which confirms the success of the specimen preparation technique in creating a completely saturated specimen. The vertical section confirms that specimen is totally saturated (no air in the pores) and consequently the water phase is continuous. Once suction is applied, $s = 1$ kPa, air can be seen to enter the specimen from the boundaries as shown in the vertical section. This is likely due to the geometric boundary effect that makes voids between grains and boundary larger than the voids between grains in the core of the specimen. Air bubbles appear when the suction reaches the "air entry value" of the material, i.e., the value of suction that causes de-saturation of the largest pores in a porous medium [25, 27, 37]. When increasing the value of suction, from $s = 1$ to $s = 1.2$ kPa, a network of connected air-filled voids is formed, indicating that air entry value for this specimen is in the range [1, 1.2] kPa. We identify the range [1, 2] kPa as the funicular domain, with air progressively filling voids

as suction increases, the largest pores being emptied of their water before the smaller ones. When studying the specimen as a whole, Fig. 8c shows that, with increasing suction, the middle part of the specimen loses water more rapidly than the top and bottom, likely due to an heterogeneity of the initial distribution of large connected voids (with bigger voids in the middle). As suction increases further, we identify the pendular domain (where the continuity of each phase is not ensured [33, 39]) in the range of suctions [2.2, 3] kPa. At the residual state ($s = 7$ kPa), the liquid phase vanishes from view at this resolution, although there is likely to be a thin film of water adsorbed on the surfaces of the grains [12], allowing continuity in the water phase—a necessary condition for the application of suction.

4 Measurement of porosity and degree of saturation

4.1 Global porosity and degree of saturation

The value of porosity of the entire specimen is classically calculated starting from a measurement of the dry mass (m_s) of the specimen and knowledge of the volume of the specimen (V_t). With knowledge of the density of the grains ($\rho_s = 2.65$), one can simply calculate the volume of the grains (V_s), and thus n. In this case, $V_t \approx 0.785$ cm^3 (cylinder of 1 cm diameter and 1 cm height), $m_s = 1.16$ g, yielding $n \approx 44\%$. The precision of this value depends on the precision of the balance used to weigh the dry specimen (which is ± 0.01 g), the loss of grains during the whole
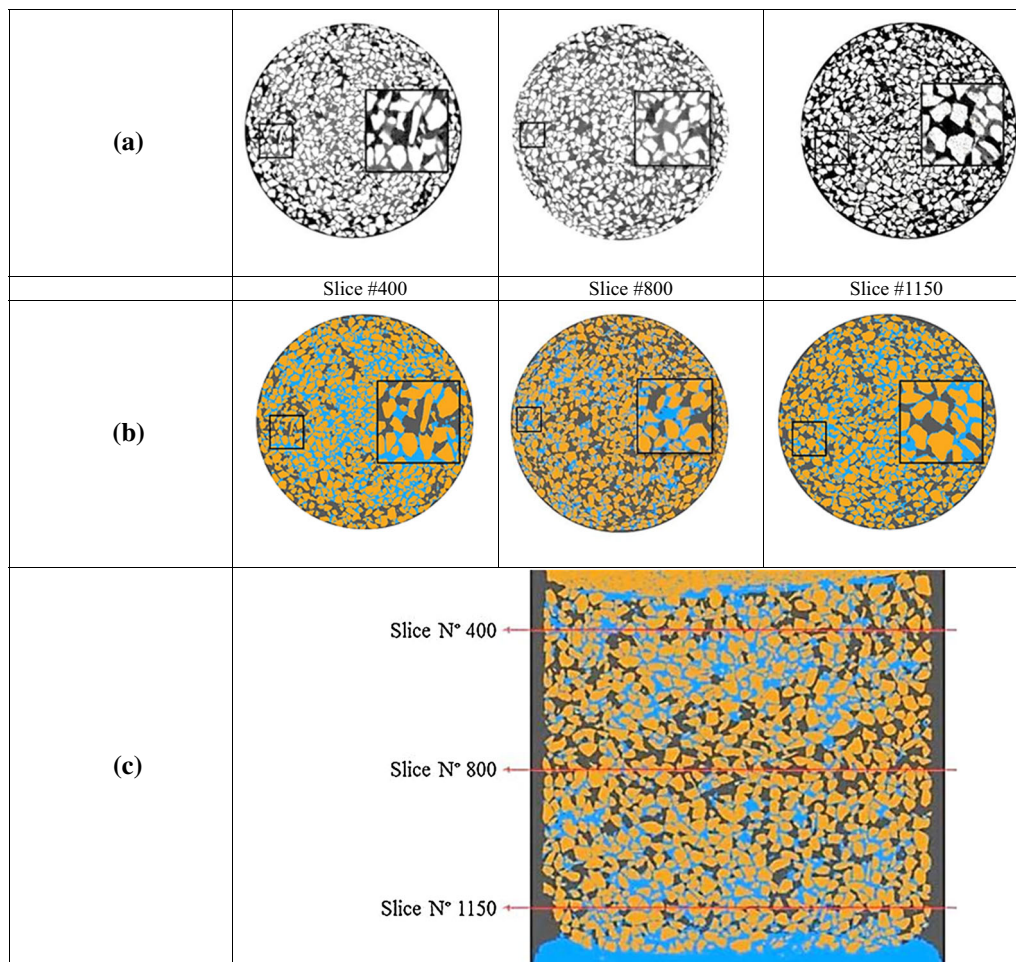
Fig. 7 Selected slices from scan #6 at $s = 2$ kPa. **a** Raw (greyscale) horizontal slices, **b** trinarized horizontal slices, and **c** trinarized vertical central slice (black = air, blue = water, orange = grain), indicating the positions of horizontal slices in **a** and **b** (colour figure online)

procedure (extracting the specimen from the cell and weighing) and the precision in calculating the volume of the cell (the height and the diameter of the specimen). Net of these errors, we estimate $a \pm 1$ error in the measurement of porosity, i.e., $n = (44 \pm 1)$ %. As for the degree of saturation, it was not possible to obtain external measurements of its evolution during drying, since the tensiometry equipment used in this case does not allow measurements of the water volume entering or exiting the specimen.

The trinarized 3D images represent an alternative and completely independent measurement of the volumes of the three phases within the specimen: V_{total} and V_{pore} can therefore be obtained simply by summing the number of voxels of each phase. Similarly, the total degree of saturation can be calculated by summing the relevant number of voxels in each phase to give $Sr = V_w/V_v$. Table 3 shows the values thus obtained porosity and degree of saturation for each trinarized image.

The porosity from the trinarized images ranges between 42.9 and 45.8%, compatible with the standard measurement of 44 ± 1%. With the assumption of no deformation of the soil skeleton, the changes in porosity between the scans must be considered a non-negligible error (somewhere in the image acquisition and processing chain) of ± 3%.

The degree of saturation from the trinarized volumes can be compared (assuming the specimens are at the same density) to the corresponding expected values from the reference WRC [32] in Table 1, see Fig. 9. The curves are relatively close in the saturated and dry regions (with a maximum deviation of 1.3%), whereas in between larger differences exist (up to 19%). These differences are very likely due to a difference in porosity (47.3 vs. 44%), but other possible reasons include different specimen preparation techniques and sizes as well as different methods of applying suction.
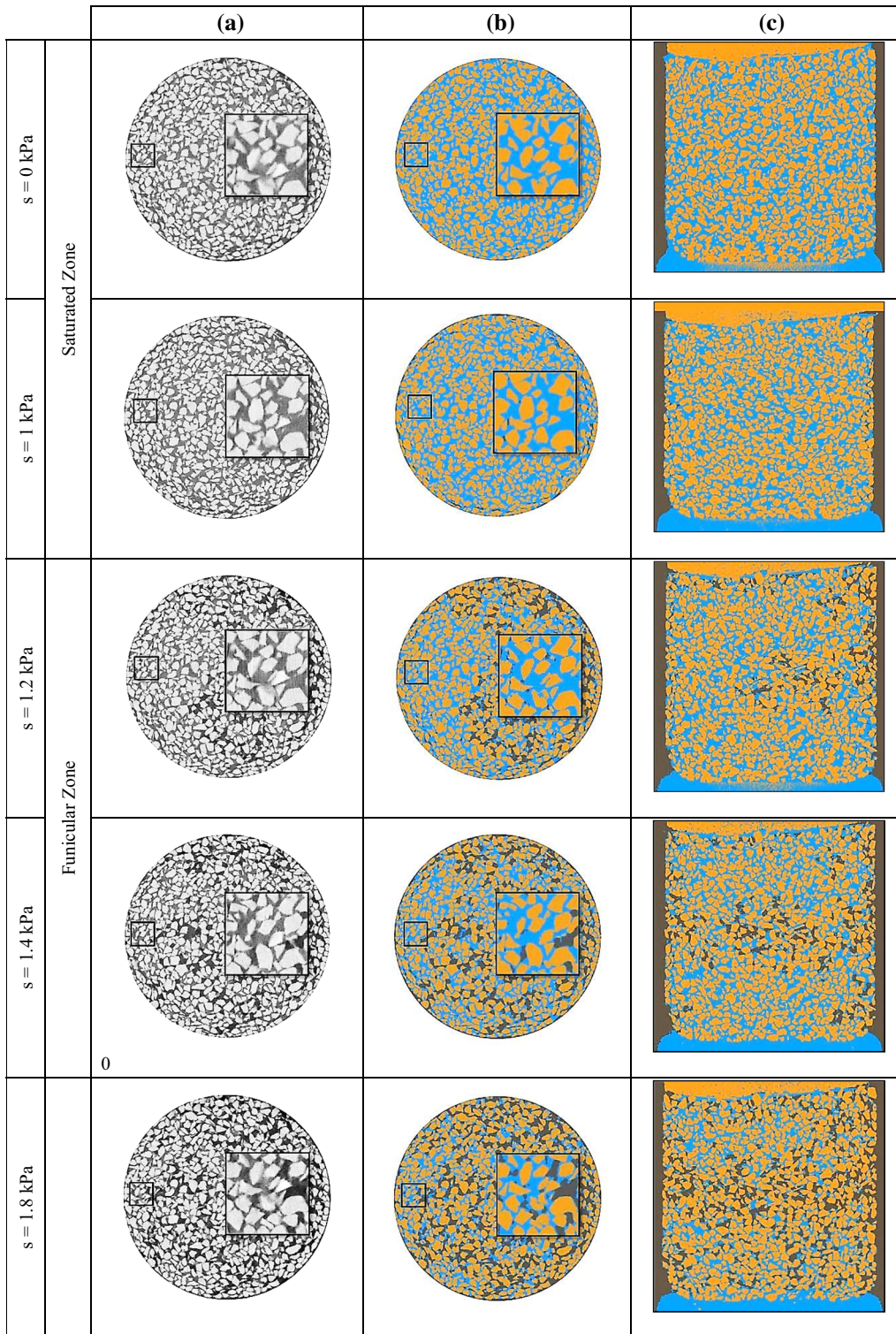
Fig. 8 Slices for suction values equal to 0, 1, 1.2, 1.4, 1.8, 2, 2.2, 2.5, 3 and 7 kPa for horizontal slice N° 800: **a** reconstructed horizontal slices, **b** trinarized horizontal slices and **c** trinarized vertical slices at the centre of the specimen
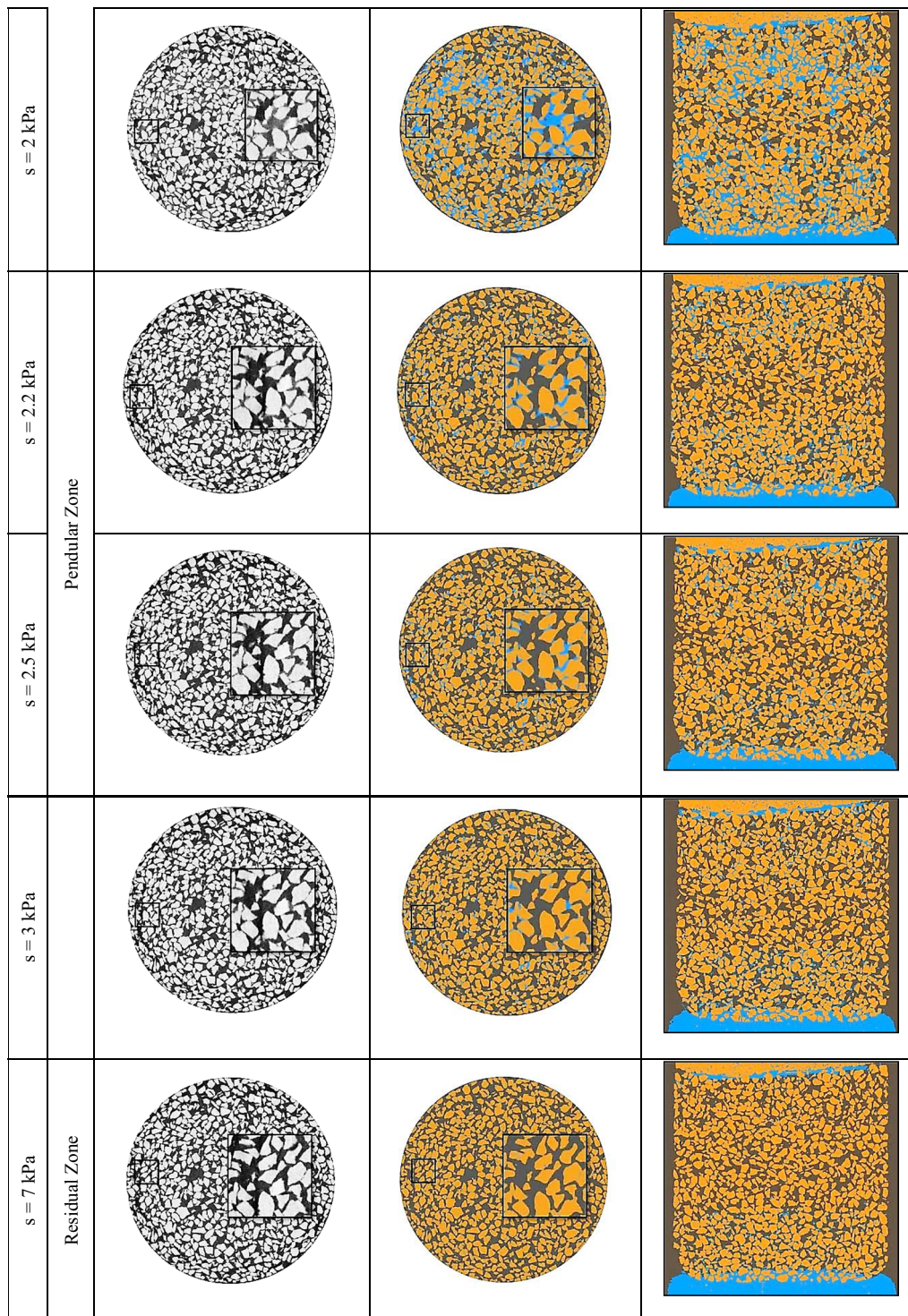
Fig. 8 continued

4.2 Microscopic (local) porosity and degree of saturation

A multi-threaded python code was developed specifically for this work. The code simply defines a regularly spaced mesh in the $1500 \times 1500 \times 1500$ pixel space ($11¼ \times 11¼ \times 11¼$ mm) of the reconstructed X-ray images. The intersections of this mesh define nodes at which porosity (n) and degree of saturation (S_r) are measured from an underlying trinarized image, in a subvolume centred on the node. In order to have a clean measurement

Table 3 Total porosity and degree of saturation measured from trinarized volumes

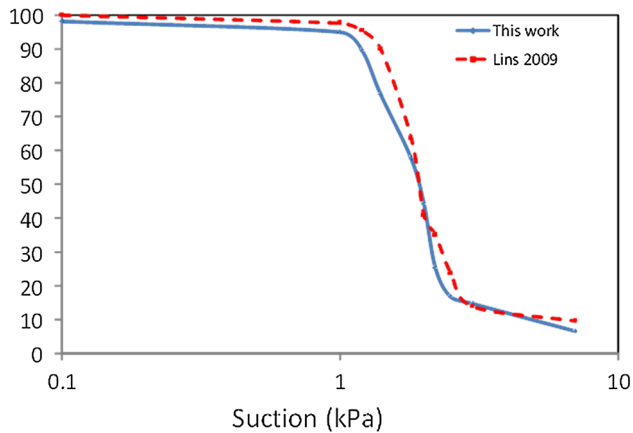| Scan	1	2	3	4	5	6	7	8	9	10
s (kPa)	0	1	1.2	1.4	1.8	2	2.2	2.5	3	7
n (%)	43.5	42.9	45.3	45.8	45.8	43.3	43.5	43.6	43.4	43.5
Sr (%)	98.2	95	80.5	74.5	57.6	44.2	22.3	16.7	14.7	6.6

Fig. 9 Comparison of water retention curves: [32] is our reference curve (see Sect. 2.5). The curve for this work corresponds to Table 3 (suction imposed and S_r measured from trinarized images)

(i.e., to avoid the top and bottom porous stone, the PMMA of the cell and surrounding air), a region of interest measuring $900 \times 900 \times 1100$ px is defined, see Fig. 10.

4.2.1 Choice of subvolume size for local analysis

To recall: the objective of defining a measurement mesh is to make a *local* measurement of the variables of interest, in order to study their spatial distribution in the specimen. With this in mind, a crucial issue is the definition of subvolume in which the variables are computed, which presents a real trade-off: a small subvolume will give highly scattered data (and at the extreme the definition of porosity in a subvolume smaller than a grain is relatively meaningless), whereas too large subvolumes will mask the local changes we aim to measure. For the variables concerned, the optimal trade-off between in size should give a representative elementary volume (REV, see [1, 3, 9, 11, 13, 23]), and since the REV size is not known a priori, the following aims to define it.

A mesh with an equal 3D spacing of 10 px is defined, giving $107 \times 90 \times 90$ measurement points within the region of interest. For each node, porosity and degree of saturation are computed on subvolumes of different sizes centred on the node, starting from a (totally meaningless)
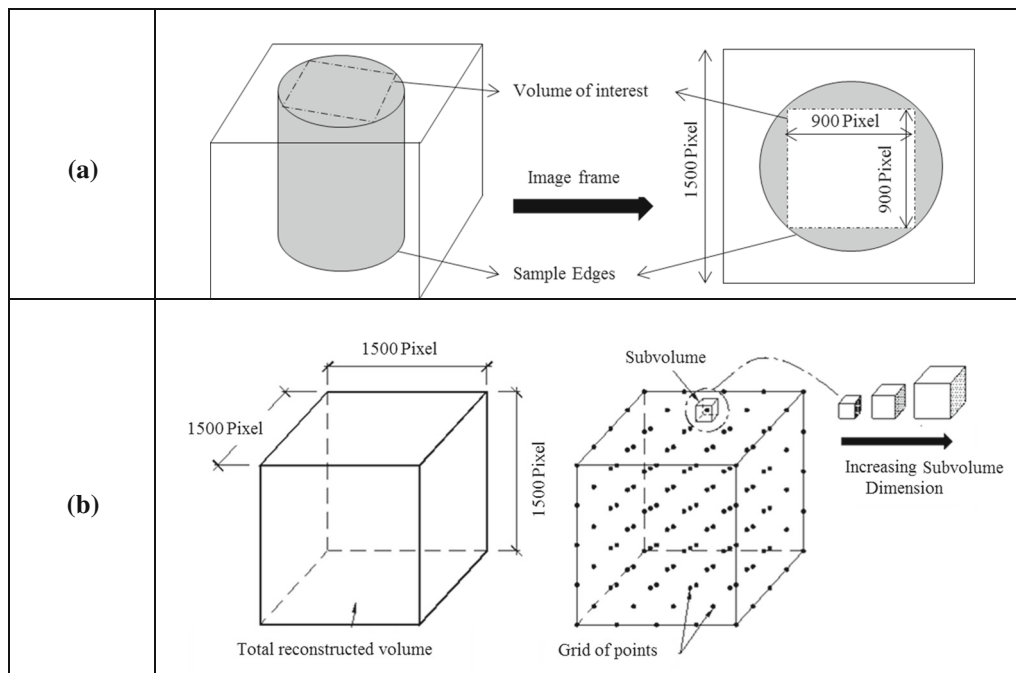

Fig. 10 a Region of interest, **b** mesh defining measurement points

(a)
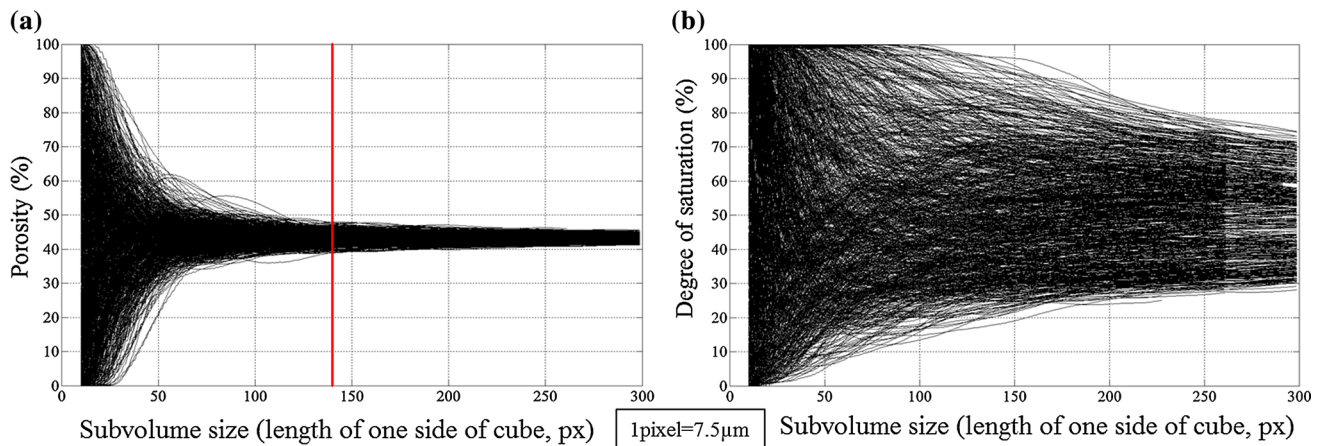

(b)

1pixel=7.5μm

Fig. 11 Porosity (left) and degree of saturation (right) as a function of subvolume size (one curve per node)

size of 1 voxel and increasing to a subvolume size of 300 px (i.e., 2¼ mm, or $6.9 \times D_{50}$). There are therefore overlaps between the subvolumes when their size is larger than 10 px. Using the trinarized volume at $s = 2$ kPa as a reference, Fig. 11 shows the results of the computation above. The left side presents the porosity measurements for all nodes, with the scatter clearly decreasing with increasing subvolume size, tending towards a global porosity of around 43%, the reading becoming stable for subvolumes larger than $100 \times 100 \times 100$ px. The same is generally true of the degree of saturation although the measurements remain much more scattered ($S_r = [30, 70\%]$ at a subvolume size of $300 \times 300 \times 300$ px, to be compared to an overall S_r of 50%) even at subvolume sizes which give a stable reading of porosity everywhere in the specimen. The reason for this is doubtlessly that water is more unequally distributed in the pores than the pores themselves and consequently the concept of an REV may not apply to the distribution of water. To investigate the relationship between degree of saturation and porosity at the small scale, a subvolume size must be chosen. We choose to set the same subvolume size everywhere in the sample and the equal for measurements of both porosity and degree of saturation, using the distribution of porosity (Fig. 11a) as a guide. Finally, a size of subvolume of $140 \times 140 \times 140$ px which yields a stable value of porosity is selected—see red bar in Fig. 11a). Note that this subvolume size corresponds to around $3 \times D_{50}$ each side. Drawing a window of 140×140 pixels in the raw images shows that a volume of this size includes several entire grains and pores (see Fig. 12).

4.2.2 Local measurements

With the subvolume size selected above, the porosity within the volume of interest is computed on a mesh defined so that there is no overlapping of the subvolumes.
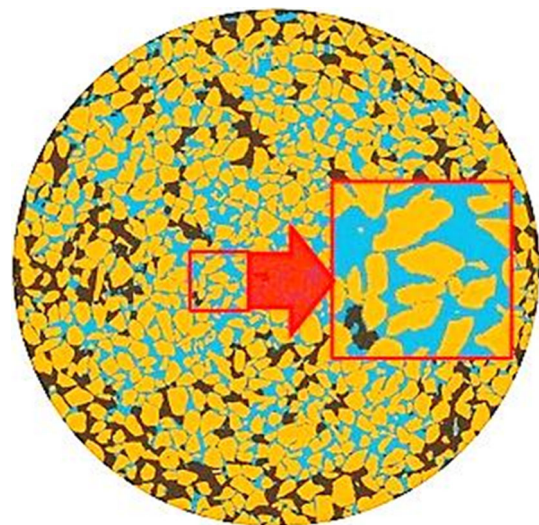

Fig. 12 Window size in 2D for REV 140 pixels

This results in $6 \times 6 \times 7 = 252$ points where the porosity is locally defined. Figure 13 presents histograms of the 252 measured porosity and degree of saturation values in all the steps of the drying test (a line representation is favoured in the figure because of the closeness of the data). Figure 13a shows that the distribution of porosity is (as expected) reasonably constant, with steps at the beginning and end of the test in very good correspondence and with three steps presenting a higher porosity of 2–3% in steps 1.4, 1.8 and 2.0 kPa (an increase of suction may well cause a real change in porosity, but this would be expected to be a monotonically *decreasing* porosity with increasing suction). The measured porosity ranges from 36 to 48% (approximately the spread of the data in Fig. 11a for subvolume = 140 px), consistent with the macroscopic porosity of 44%. Please note that this is roughly the range of minimum to maximum porosity for Hostun sand. Figure 13b also presents a series of histograms, with filled bars
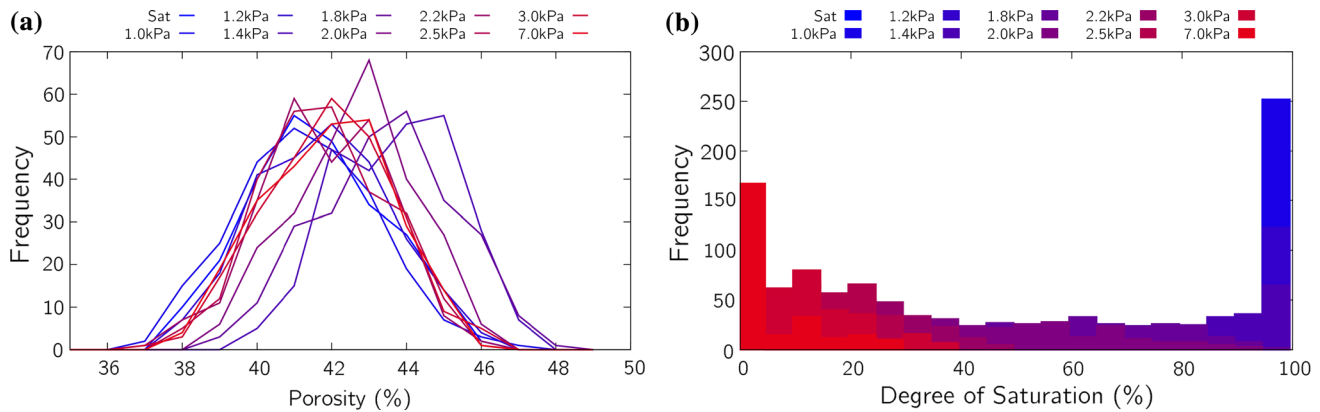
Fig. 13 a (Line) histogram of locally measured porosities from all scanned states (bin size = 1% porosity). **b** (Bar) histogram of locally measured degree of saturation from all scanned states (bin size = 5% Sr)

rather than curves for clarity. At the beginning of the drying test, the degree of saturation is in the top bin from 95 to 100%. As the sample is dried, the mean value necessarily decreases, and the spread of the degree of saturation increases, which is interpreted as a result of both a distribution of throat sizes and also of "patchy" saturation (with coexistence of essentially dry and saturated regions including multiple grains within the specimen). At the maximum suction, the distribution is chiefly in the bottom bin 0–5%; however, there is some signal until the 30% bin.

Figure 14 presents a selection of 5 different states analysed in the drying experiment, from the saturated state to the driest. For each different state, a diametrical slice through the trinarized volume is presented, with the region of interest highlighted, with the corresponding field of porosity and degree of saturation presented with a colour map. A slight vertical organization of the porosity can be seen with a higher porosity section in the middle of the region of interest. As before, the porosity can be seen to change from state to state, giving some idea of the accuracy of the method. The local measurement of degree of saturation shows a dramatic change (as expected from the macro results) from a totally saturated state to a practically dry one. In states 2.0 kPa onwards, a strong vertical organization of the degree of saturation is clearly visible, with darker (and therefore dryer) areas appearing in the middle of the specimen in the zone with higher porosity.

In order to study the vertical organization of the porosity and degree of saturation more effectively, the 6 × 6 local measurements of both quantities at equal height are averaged together and presented in Fig. 15. Again, the 1.2, 1.4 and 2.0 kPa porosity measurements appear to be a little higher than the rest, but in any case there is a zone in the middle of the region of interest with higher porosity, to which the degree of saturation measurements are sensitive.

The local relationship between degree of saturation and porosity which is noticeable here due to the slight

inhomogeneity of the specimen hints at the possibility of the verification of this relationship at the micro-scale. Figure 16 presents a first step in this direction, combining all the local measurements made herein (please note that the slight change in suction due to the height of the specimen is not taken in account here, i.e., the suction is the globally applied one at the mid-height of the specimen). Since this experiment is a monotonic drying experiment, a univocal relationship could be expected between these quantities (the presence of cycles and therefore hysteresis would render this impossible). This said, there is a significant amount of scatter in this plot that clearly indicates that some ingredients are missing in the relationship between these quantities, which are doubtlessly related to the microscopic throat geometry, which may one day be obtained from the trinarized images.

In order to investigate the spread of data further, in Fig. 17, taken from [22], local measurements of porosity and degree of saturation are binned by frequency and shown as a contour map with colours representing frequency. This is shown for the states $s = 1.8$ kPa and $s = 2.5$ kPa; please note that the variation in suction due to gravity is not taken into account. For completeness, the frequency distribution of both variables is also shown (consistent with 13a and 13b). The general trend observed in macroscopic measurements remains valid, but instead of having a unique and linear relation between the two variables, the local measurements have a significant scatter around the linear trend (see [38] for a complete experimental characterization at the macro-scale).

5 Conclusions

In this work, we have used X-ray tomography to make 3D images of a drying process in a small specimen of sand. Quantitative image analysis has been applied to each single
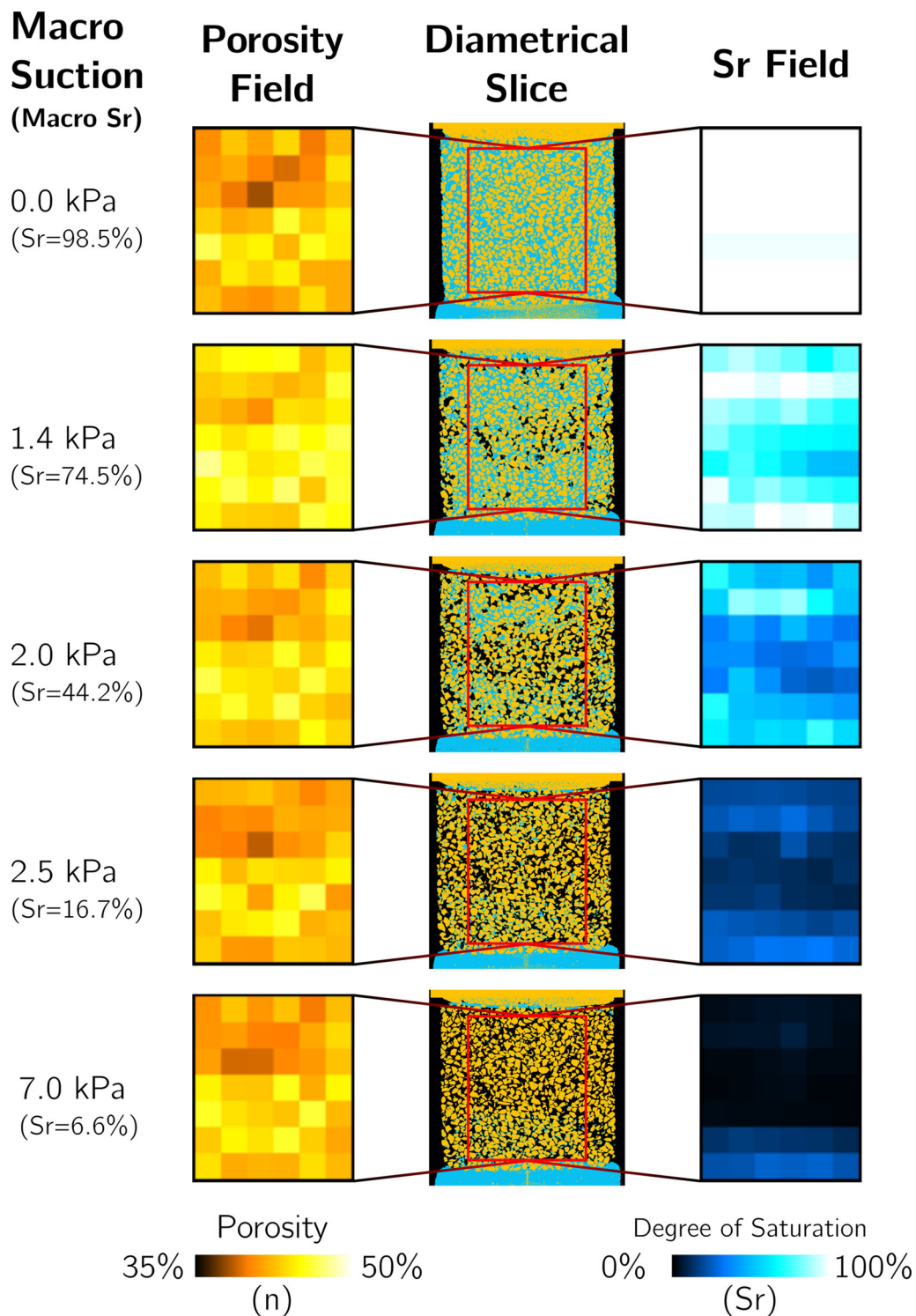
Fig. 14 Vertical sections of porosity field, trinarized image and degree of saturation field (all lookup tables are coherent) presented for a selected number of saturation states

image, allowing the drying process to be followed in 3D. From the X-ray transparent retention cell, to the experimental protocol, scanning and image analysis techniques, this paper presents an original, complete and reproducible

experimental methodology for the study (at the grain scale) of water retention behaviour in sand.

Some technical improvements are currently under way: a new cell is being developed with an inbuilt burette for
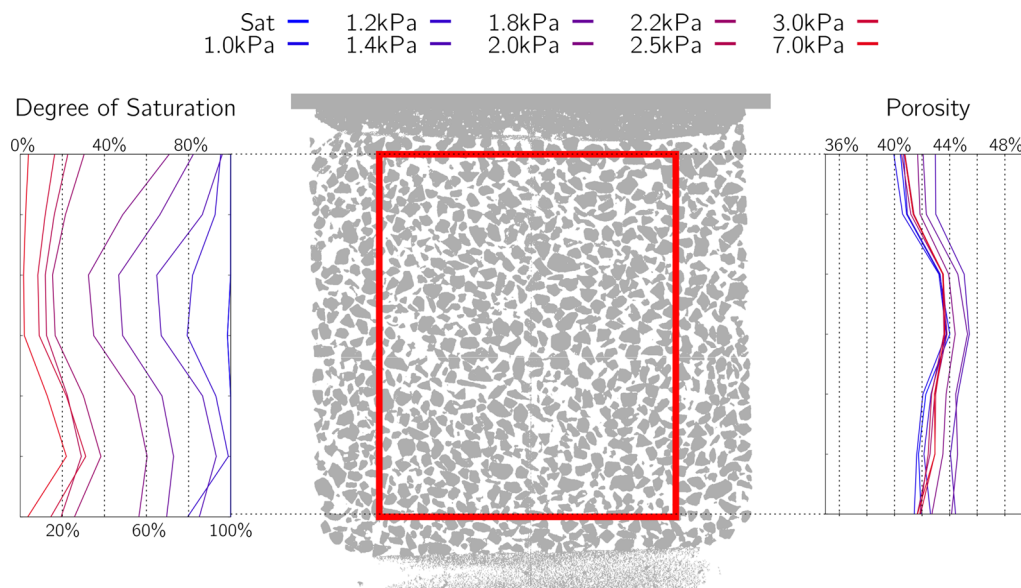
Fig. 15 Vertical evolution of porosity and degree of saturation throughout the drying test
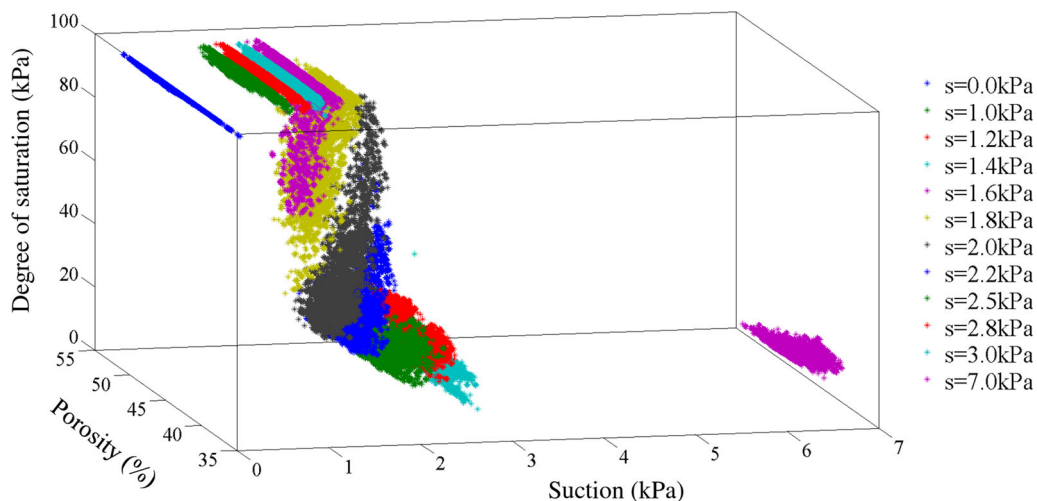

Fig. 16 3D plot of the local measurements of degree of saturation, porosity against their respective macroscopic suction values

suction control to overcome some minor difficulties encountered in the pressure–volume control due to temperature effects. Moreover, experiments on spherical grains are also planned, allowing both high-precision quantification with [40] and more direct comparisons with grain-based simulations [16, 34, 50, 52].

The ability to observe the change in water distribution at the grain scale allows the experimentalist to explore the correspondence between macro-scale concepts (degree of saturation, porosity, etc.) and the reality at the grain scale. In the case of perfect homogeneity, this extra information does not bring much; however, given that heterogeneity is the rule rather than the exception in real granular media, these tools open the possibility of a quantitative connection between the scales that will be extremely valuable for future (multiscale) modelling work in the area of unsaturated soil mechanics. This sort of experiment provides information which is simply inaccessible using standard tools, for example:

1. In the small specimen studied, the distribution of water at some levels of suction is very heterogeneous—small differences in porosity result in large changes of degrees of saturation. This "patchy" saturation, which in some cases means totally saturated and practically dry regions coexisting in the specimen for a given value of imposed suction, really begs the question of the meaning of a macroscopic degree of saturation in this case.
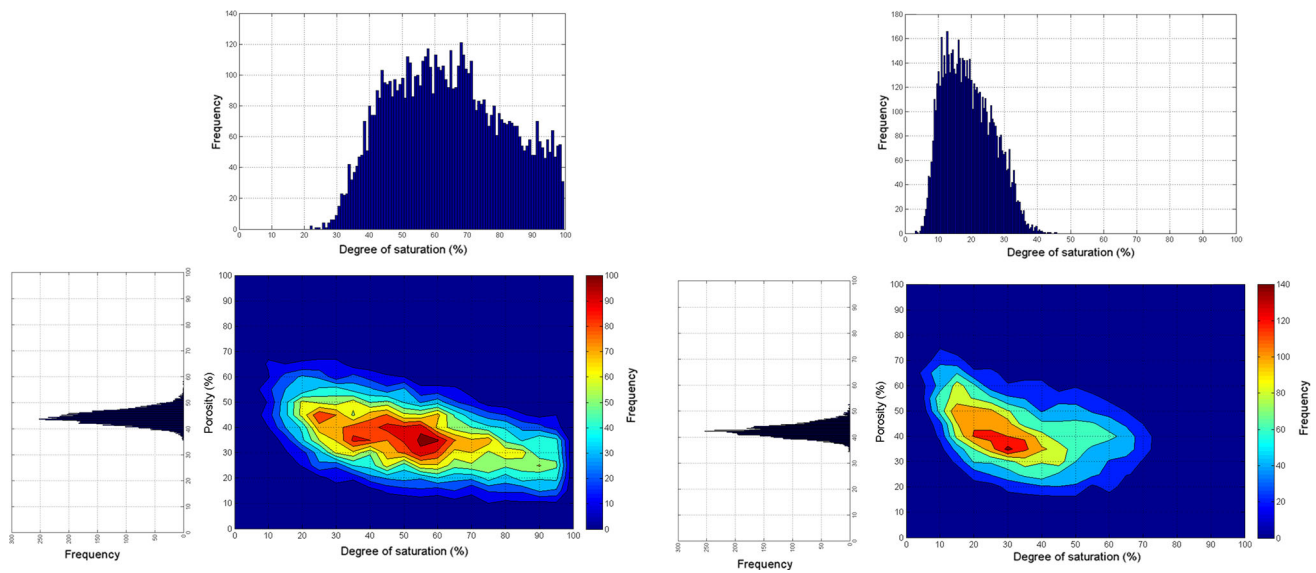
Fig. 17 Frequency maps of local measurements of porosity and degree of saturation for constant suctions of $s = 1.8$ kPa on the left and $s = 2.5$ kPa on the right from [22]

2. The quantitative and well-verified relationship between degree of saturation and porosity in sand still exists at the small scale, but a significant scatter around the linear trend can be observed; this indicates that some other ingredients must be added to the relationship (such as pore/grain geometry).

These experimental findings may begin to question conventional understanding of the hydraulics of partially saturated sand, and in some cases, hydro-mechanics couplings. A clear perspective for this work is therefore to add mechanical deformation to the picture, in the style of [2, 20, 21]. A triaxial cell—compatible with X-ray tomography—for unsaturated soil has been developed with this in mind. Returning to the cell presented in this work, it is of clear interest to use the techniques presented to investigate the phenomenon of hydraulic hysteresis, i.e., the well-known discrepancy between wetting and drying paths (ink-bottle effect, etc.) at the grain scale, see [26] for a recent PhD on this subject.

Finally, a very exciting technical perspective for this work is the use of neutron imaging [29, 30] which is highly sensitive to water, thus increasing the quality of measurement of the distribution of water. In the case where mechanical loads are applied to the specimen, X-ray may be coupled with neutrons to also follow the deformation of the solid skeleton.

References

1. Al-Raoush R, Papadopoulos A (2010) Representative elementary volume analysis of porous media using X-ray computed tomography. Powder Technol 200(1):69–77

2. Andò E, Hall SA, Viggiani G, Desrues J, Bésuelle P (2012) Grain-scale experimental investigation of localised deformation in sand: a discrete particle tracking approach. Acta Geotech 7(1):1–13

3. Andò E (2013) Experimental study of the evolution of the microstructure of a granular medium under mechanical loading using tomography X-ray. PhD thesis, Laboratoire 3SR, Grenoble, France

4. Andrade JE, Borja RI (2006) Capturing strain localization in dense sands with random density. Int J Numer Methods Eng 67(11):1531–1564

5. Arya LM, Paris JF (1981) A physicoempirical model to predict the soil moisture characteristic from particle-size distribution and bulk density data. Soil Sci Soc Am J 45(6):1023–1030

6. Borja RI, Andrade JE (2006) Critical state plasticity. Part VI: meso-scale finite element simulation of strain localization in discrete granular materials. Comput Methods Appl Mech Eng 195(37–40):5115–5140

7. Borja RI, Song X, Rechenmacher AL, Abedi S, Wu W (2013) Shear band in sand with spatially varying density. J Mech Phys Solids 61(1):219–234

8. Borja RI, Song X, Wu W (2013) Critical state plasticity. Part VII: triggering a shear band in variably saturated porous media. Comput Methods Appl Mech Eng 261–262:66–82

9. Bruchon JF, Pereira JM, Vandamme M, Lenoir N, Delage P, Bornert M (2013) Full 3D investigation and characterisation of capillary collapse of a loose unsaturated sand using X-ray CT. Granul Matter 15(6):783–800

10. Canou J (1989) Contribution à L'étude et à l'élaboraion des propriétés de liquéfaction d'un sable. PhD thesis, CERMES-ENPC, Paris, France

11. Carminati A, Kaestner A, Lehmann P, Flühler H (2008) Unsaturated water flow across soil aggregate contacts. Adv Water Resour 31(9):1221–1232
12. Colliat JL, Desrues J, Foray P (1988) Triaxial test under elevated cell pressure, ASTM STP N° 977, advanced triaxial testing for soils and rocks, pp 290–310
13. Costanza-Robinson MS, Estabrook BD, Fouhey DF (2011) Representative elementary volume estimation for porosity, moisture saturation, and air-water interfacial areas in unsaturated porous media: data quality implications. Water Resour Res 47(7)
14. Culligan KA, Wildenschild D, Christensen BSB, Gray WG, Rivers ML (2006) Pore-scale characteristics of multiphase flow in porous media: a comparison of air–water and oil–water experiments. Adv Water Resour 29(2):227–238
15. Degny É (1984) Etude du comportement d'un sable dense à l'aide d'une presse tridimensionnelle. PhD thesis, Laboratoire 3SR, Grenoble, France
16. Duriez J, Wan R (2015) Effective stress in unsaturated granular materials: micro-mechanical insights. Coupled Probl Sci Eng VI:1232–1242
17. Feldkamp LA, Davis LC, Kress JW (1984) Practical cone-beam algorithm. JOSA A 1(6):612–619
18. Fredlund DG, Xing A (1994) Equations for the soil-water characteristic curve. Can Geotech J 31(4):521–532
19. Hashemi MA, Khaddour G, François B, Massart TJ, Salager S (2014) A tomographic imagery segmentation methodology for three-phase geomaterials based on simultaneous region growing. Acta Geotech 9(5):831–846
20. Higo Y, Oka F, Kimoto S, Sanagawa T, Matsushima Y (2011) Study of strain localization and microstructural changes in partially saturated sand during triaxial tests using microfocus X-ray CT. Soils Found 51(1):95–111
21. Higo Y, Oka F, Sato T, Matsushima Y, Kimoto S (2013) Investigation of localized deformation in partially saturated sand under triaxial compression using microfocus X-ray CT with digital image correlation. Soils Found 53(2):181–198
22. Higo Y, Morishita R, Kido R, Khaddour G, Salager S (2015) Local water-retention behaviour of sand during drying and wetting process observed by micro X-ray tomography with trinarisation. Jpn Geotech Soc Spec Publ 2(16):635–638
23. Hopmans JW, Nielsen DR, Bristow KL (2002) How useful are small-scale soil hydraulic property measurements for large-scale vadose zone modeling? Geophys Monogr 129:247–258
24. Jarvis NJ, Jansson PE, Dik PE, Messing I (1991) Modelling water and solute transport in macroporous soil. I. Model description and sensitivity analysis. J Soil Sci 42(1):59–70
25. Khaddour G, Andò E, Salager S, Bésuelle P, Viggiani C, Hall S, Desrues J (2013) Application of X-ray tomography to the characterisation of grain-scale mechanisms in sand. In: Multiphysical testing of soils and shales, pp 195–200. Springer, Berlin
26. Khaddour G (2015) Multi-scale charaterisation of the hydro-mechecanical behaviour of unsaturated sand: water retention and triaxial responses. PhD thesis, Laboratoire 3SR, Grenoble, France
27. Khalili N, Russell A, Khoshghalb A (eds) (2014) Unsaturated soils: research & applications. CRC Press, Boca Raton
28. Kaestner A et al (2007) Mapping the 3D water dynamics in heterogeneous sands using thermal neutrons. Chem Eng J 130(2):79–85
29. Kim FH, Penumadu D, Hussey DS (2011) Water distribution variation in partially saturated granular materials using neutron imaging. J Geotech Geoenviron Eng 138:147–154
30. Kim FH, Penumadu D, Gregor J, Kardjilov N, Manke I (2012) High-resolution neutron and X-ray imaging of granular materials. J Geotech Geoenviron Eng 139(5):715–723
31. Li XS (2005) Modelling of hysteresis response for arbitrary wetting/drying paths. Comput Geotech 32(2):133–137
32. Lins I (2009) Hydro-mechanical properties of partially saturated sand. PhD thesis, Engineer. Faculty of Civil Engineering, Bochum, Germany
33. Lozano AL, Cherblanc F, Cousin B, Bénet JC (2008) Experimental study and modelling of the water phase change kinetics in soils. Eur J Soil Sci 59(5):939–949
34. Nikooee E, Habibagahi G, Hassanizadeh SM, Ghahramani A (2013) Effective stress in unsaturated soils: a thermodynamic approach based on the interfacial energy and hydromechanical coupling. Transp Porous Media 96(2):369–396
35. Nuth M, Laloui L (2008) Advances in modelling hysteretic water retention curve in deformable soils. Comput Geotech 35(6):835–844
36. Riedel I, Andò E, Salager S, Bésuelle P, Viggiani G (2012) Water retention behavior explored by X-ray CT analysis. Springer series in unsaturated soils: research and applications 2012, part 1, pp 81–88. https://doi.org/10.1007/978-3-642-31116-1_11
37. Romero E, Simms PH (2008) Microstructure investigation in unsaturated soils: a review with special attention to contribution of mercury intrusion porosimetry and environmental scanning electron microscopy. Geotech Geol Eng 26(6):705–727
38. Salager S, El Youssoufi MS, Saix C (2010) Definition and experimental determination of a soil-water retention surface. Can Geotech J 47(6):609–622
39. Salager S, Khaddour G, Charrier P, Desrues J (2014) An investigation into unsaturated states of granular media using X-ray computed tomography. Unsaturated soils: research & applications. CRC Press, Boca Raton, pp 703–709
40. Song X, Borja RI (2014) Mathematical framework for unsaturated flow in the finite deformation range. Int J Numer Methods Eng 97(9):658–682
41. Song X, Borja RI (2014) Finite deformation and fluid flow in unsaturated soils with random heterogeneity. Vad Zone J. https://doi.org/10.2136/vzj2013.07.0131
42. Tengattini A, Andò E (2015) Kalisphera: an analytical tool to reproduce the partial volume effect of spheres imaged in 3D. Meas Sci Technol 26(9):095606
43. Townend J, Reeve MJ, Carter A (2000) Water release characteristic. Soil and environmental analysis: physical methods. Water release characteristic, 2nd edn. Marcel Dekker, New York, pp 95–140
44. Vanapalli SK, Fredlund DG, Pufahl DE (1999) The influence of soil structure and stress history on the soil–water characteristics of a compacted till. Geotechnique 49(2):143–159
45. Van Genuchten MT (1980) A closed-form equation for predicting the hydraulic conductivity of unsaturated soil. Soil Sci Soc Am J 44:892–898
46. Viggiani G, Hall SA (2008) Full-field measurements, a new tool for laboratory experimental geomechanics. In: Fourth symposium on deformation characteristics of geomaterials, vol 1, pp 3–26. IOS Press, Amsterdam
47. Viggiani G, Santamarina JC, Takano D, Andò E (2014) Laboratory X-ray tomography: a valuable experimental tool for revealing processes in soils
48. Wildenschild D, Culligan KA, Christensen BS (2004) Application of X-ray micro tomography to environmental fluid flow problems. In: Optical science and technology, the SPIE 49th annual meeting, pp 432–441. International Society for Optics and Photonics
49. Wildenschild D, Sheppard AP (2013) X-ray imaging and analysis techniques for quantifying pore-scale structure and processes in subsurface porous medium systems. Adv Water Resour 51:217–246
50. Xu J, Louge MY (2015) Statistical mechanics of unsaturated porous media. Phys Rev E 92(6):062405

51. Yoshimoto N, Orense RP, Tanabe F, Kikkawa N, Hyodo M, Nakata Y (2011) Measurement of degree of saturation on model ground by digital image processing. Soils Found 51:167–177

52. Yuan C, Chareyre B, Darve F (2015) Pore-scale simulations of drainage in granular materials: finite size effects and the representative elementary volume. Adv Water Resour